

Walther
Meißner
Institut



BAYERISCHE
AKADEMIE
DER
WISSENSCHAFTEN

Exciting the Spin Transitions of ^{167}Er : CaWO_4 with Propagating Microwaves via Superconducting Electrical Circuits

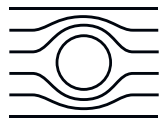
Hayden Nathanael Tanis

Technische Universität München, School of Computation,
Information, and Technology

Walther Meißner Institut der Bayerischen Akademie der
Wissenschaften

Garching, Germany

August 2025



Walther
Meißner
Institut



BAYERISCHE
AKADEMIE
DER
WISSENSCHAFTEN

SCHOOL OF COMPUTATION, INFORMATION AND
TECHNOLOGY

TECHNISCHE UNIVERSITÄT MÜNCHEN

Bachelor's Thesis

**Exciting the Spin Transitions of
 ^{167}Er : CaWO₄ with Propagating Microwaves
via Superconducting Electrical Circuits**

Author: Hayden Nathanael Tanis
Examiner: Prof. Dr. Kai Müller
Supervisor: Dr. Nadezhda Kukharchyk
Submission Date: 03/08/2025

Abstract

Quantum information processing exploits quantum mechanical phenomena like superposition and entanglement to enable computational capabilities beyond classical systems. However, superconducting qubits in current implementations suffer from short coherence times. Hybrid quantum systems address this by interfacing superconducting quantum processors with quantum memory devices. The physical implementation of quantum memories requires materials with naturally long coherence times. Rare-earth ions doped into crystal hosts have emerged as attractive quantum memory candidates due to their well-isolated 4f subshells and long coherence times.

This work investigates the spin transitions of erbium ions doped into calcium tungstate (CaWO_4) crystals coupled to superconducting coplanar waveguides. We characterize erbium's spin transitions and their spin-lattice relaxation times using broadband electron paramagnetic resonance spectroscopy under varying magnetic fields. Zero-field spectroscopy measurements identified the hyperfine transitions, while field-dependent measurements revealed their magnetic field dependencies. Saturation recovery measurements in cryogenic environments probed the relaxation dynamics of individual spin transitions. The results demonstrate long relaxation times for hyperfine transitions of up to a few hundred seconds, indicating extended excited-state lifetimes and suggesting the system's potential for long-duration quantum state storage.

Kurzzusammenfassung

Die Quanteninformationsverarbeitung nutzt quantenmechanische Phänomene wie Superposition und Verschränkung, um Rechenkapazitäten zu ermöglichen, die über klassische Systeme hinausgehen. Jedoch leiden supraleitende Qubits in aktuellen Implementierungen unter kurzen Kohärenzzeiten. Hybride Quantensysteme adressieren dies, indem sie supraleitende Quantenprozessoren mit Quantenspeichergeräten koppeln, was Materialien mit natürlich langen Kohärenzzeiten erfordert. Seltene-Erden-Ionen, die in Kristallwirte dotiert sind, haben sich aufgrund ihrer gut isolierten 4f-Unterschalen und außergewöhnlich langen Kohärenzzeiten als attraktive Quantenspeicherkandidaten erwiesen.

Diese Arbeit untersucht die Spinübergänge von Erbium-Ionen, die in Kalzium-wolframat (CaWO_4)-Kristalle dotiert und an supraleitende koplanare Wellenleiter gekoppelt sind. Wir charakterisieren Spinübergänge von Erbium und deren Spin-Gitter-Relaxationszeiten mittels Elektronenspinresonanz-Spektroskopie unter variierenden Magnetfeldern. Nullfeld-Spektroskopiemessungen identifizieren die Hyperfeinübergänge, während feldabhängige Messungen deren Magnetfeldabhängigkeiten aufzeigen. Sättigungswiederherstellungsmessungen in kryogenen Umgebungen untersuchten die Relaxationsdynamik einzelner Spinübergänge. Die Ergebnisse zeigen lange Relaxationszeiten bis zu hunderten Sekunden von Hyperfeinübergängen. Dies zeigt, dass angeregte Zustände lange erhalten bleiben und das System daher gut als Quantenspeicher geeignet ist.

Contents

Abstract	ii
Kurzzusammenfassung	iii
1 Introduction	1
2 Theory: Rare-earth Physics and Spin Dynamics	4
2.1 Introduction to rare-earth Elements	4
2.2 Erbium Dopants in Calcium Tungstate	5
2.2.1 Host Crystal: CaWO ₄	5
2.2.2 Energy Structure of Erbium	6
2.3 Spin Dynamics	9
2.3.1 Two Level Quantum Systems and the Bloch Sphere	9
2.3.2 Spin Relaxation Processes	10
3 Experimental Methodology	13
3.1 Broadband Electron Paramagnetic Resonance Spectroscopy with Superconducting Coplanar Waveguides	13
3.2 Measurement Setup	15
3.3 T ₁ Measurement via Saturation Recovery	18
4 Results	21
4.1 Zero Magnetic Field Spectroscopy	21
4.2 Magnetic Field Sweeps	24

Contents

4.3 Spin-Lattice Relaxation Measurements	25
4.3.1 Correction and Analysis Procedure	27
4.3.2 Field Dependent Measurements	32
5 Conclusion	37
List of Figures	39
List of Tables	40
Bibliography	41
Acknowledgments	44

CHAPTER 1

Introduction

While the first quantum revolution gave humanity transistors, lasers, and MRI machines that are essential to today's society, the second quantum revolution promises to fundamentally rewrite the rules of computation, communication, and measurement itself. The laws of quantum mechanics enable the development of a new kind of computation called quantum computing or, in a larger sense, quantum information processing (QIP) [1].

In quantum information processing, quantum bits (qubits), which exploit quantum mechanical phenomena such as interference and superposition, replace classical bits (0's and 1's) to carry and manipulate information to perform computational tasks. Quantum computing takes advantage of quantum mechanical phenomena such as superposition and entanglement to perform tasks such as factoring and simulations that are computationally beyond the reach of classical algorithms. Ultimately, the long-term aim of current research in quantum computing is to achieve an interconnected network of quantum computers that shares similarities with the Internet of today. This is achieved by the distribution of entanglement, which interconnects quantum computers [10].

To develop these innovative technologies, researchers are exploring various advanced physical platforms to realize qubits. One of the most promising candidates is superconducting quantum circuits, which operate in the microwave range at zero magnetic fields and in cryogenic temperatures [20]. The scalability and flexibility of superconducting qubits allow scientists and engineers to advance the field of quantum computing and create the essential technologies for designing, controlling, and reading

out quantum systems, such as multiqubit processors [9, 12, 16, 22].

Despite their promise, one critical weakness of superconducting qubits is their short coherence times. Long coherence times, i.e., the ability to store quantum states for a long time before the loss of quantum properties due to interaction with the environment, are an important metric in quantum information technology. Longer coherence times ensure the reliability of computation, as well as fidelity and scalability of quantum processors [8]. In order to push the field of quantum computing further, a solution needs to be implemented to solve the problem regarding short coherence times in superconducting qubits. For this reason, in recent years interest has been shown in the development of hybrid quantum systems which interface a superconducting quantum circuit acting as a quantum processor to a device called quantum memory [20].

Quantum memories are systems whose primary task is to store quantum information/quantum states and preserve the quantum properties, such as entanglement and superposition, for later retrieval. In hybrid quantum systems, natural entities with long coherence times take the role of quantum memory to complement the short coherence time of quantum processors based on superconducting qubits. Several platforms are currently being investigated for their use as quantum memory, for example, spin ensembles such as donors in silicon and rare-earth doped crystals [9]. In particular, rare-earth doped crystals are a very promising platform to realize quantum memories due to the long coherence times of their hyperfine and optical transitions. For example, [5] has shown a 23 ms spin coherence time of Erbium doped in crystals. Furthermore, erbium ions possess optical transitions at $\simeq 1.5 \mu\text{m}$ that are widely used in the current standard telecommunication bands [9, 13, 10, 16].

While these quantum memory applications show great promise, the successful implementation of rare-earth systems in hybrid quantum devices requires a fundamental understanding of their spin dynamics and relaxation mechanisms. The performance of quantum memories depends on the coherence properties of the medium, which are directly governed by spin relaxation processes. Specifically, spin-lattice relaxation (T_1) determines how long quantum information can be stored before relaxation to thermal equilibration destroys the stored state, while spin-spin relaxation (T_2) sets limits on the coherence time during storage and retrieval operations. Understanding these relaxation mechanisms and their interaction with external parameters such as magnetic fields is therefore crucial for determining optimal operating conditions for practical quantum devices.

This thesis aims specifically to investigate erbium ions doped into calcium tungstate (CaWO_4) crystals. We utilize a hybrid quantum system where the rare-earth spins are coupled to a superconducting coplanar waveguide in cryogenic environments. The primary objective is to characterize the spin relaxation mechanisms in the spin

transitions in these rare-earth systems.

The choice of erbium-doped calcium tungstate represents an ideal platform for studying quantum spin dynamics due to the well-isolated 4f electronic states of erbium and the crystalline environment provided by the tungstate host. To understand the experimental observations and interpret the measured relaxation dynamics, a comprehensive theoretical foundation is essential. Therefore, chapter 2 establishes the theoretical foundation for understanding the physics of rare-earth ions, with particular emphasis on erbium. The chapter opens with an examination of the electronic structure and characteristics of rare-earth ions. An emphasis is given on the energy structure of erbium doped in crystals, specifically in calcium tungstate (CaWO_4). The latter portion of the second chapter focuses on spin dynamics and spin relaxation. A brief introduction to two-level quantum systems will be given. We will then discuss the various mechanisms through which excited spin states return to thermal equilibrium. We analyze spin-lattice (T_1) and spin-spin (T_2) relaxation processes. This theoretical framework establishes the context for understanding the relaxation measurements and their temperature and magnetic field dependencies presented in the experimental chapters that follow.

Chapter 3 provides an overview of broadband electron paramagnetic resonance (BEPR) spectroscopy employing superconducting coplanar waveguides, the primary experimental technique utilized in this work. The chapter begins with a concise description of the EPR method and its implementation with superconducting coplanar waveguide structures. We will then present a description of the experimental setup used for this work, including the cryogenic setup and microwave components. The chapter concludes with a discussion of the saturation recovery technique, a time-domain method used to observe spin-lattice relaxation processes. We discuss both the theoretical principles underlying this approach and its practical implementation within our experimental framework.

In Chapter 4, the results of various measurements will be presented. Firstly, the results of zero-field spectroscopy will be presented, which provide an overview of the behavior of several hyperfine transitions in the spin system. Afterward, magnetic field sweeps will be conducted, in which the spectroscopy will be carried out under different magnetic field strengths in order to see how the transition frequencies change with respect to the magnetic field. We will then present the results of the saturation recovery measurements, by which we can extract the spin-lattice relaxation time of the spin transitions. The final section of this chapter is dedicated to the magnetic field dependency of a hyperfine transition, where we will present results of the saturation recovery measurement done under the influence of different magnetic fields in the low field regime. The last chapter will then provide a comprehensive summary of this work and provide a conclusion.

CHAPTER 2

Theory: Rare-earth Physics and Spin Dynamics

2.1 Introduction to rare-earth Elements

Rare-earth elements are a group of 17 metals in the periodic table, consisting of Scandium, Yttrium, and 15 other elements called Lanthanides. Lanthanides form a significant subset of rare-earth elements. The electron configuration of Lanthanides is built on top of the noble gas xenon (Xe , $Z = 54$) which has the configuration $1s^2 2s^2 2p^6 3s^2 3p^6 4s^2 3d^{10} 4p^6 5s^2 4d^{10} 5p^6$. Lanthanide ions are distinguished by the filling of the 4f subshell in their electron configurations. Table 2.1 provides an overview of Lanthanides alongside the electron configuration of their trivalent ions¹ and their atomic number.

In solids, lanthanides typically exist in the form of trivalent rare-earth ions (RE^{3+}) with partially filled 4f subshells. Generally, trivalent rare-earth ions follow the electron configuration of $[Xe]4f^N$, where N denotes the number of electrons in the 4f subshell. The range of electrons occupying the 4f subshell spans from 0 in Lanthanum to 14 in Lutetium.

The speciality of rare-earth ions is the shielding of their 4f electrons by the electrons in the 5s and 5p shells. This Faraday-cage-like structure protects the 4f electrons from external perturbations and therefore causes the system to have narrow 4f-4f transition linewidths and very good coherence times. As an example, 23 ms coherence time has been observed in Erbium ions embedded in scheelite crystals. [5]. For this reason,

¹The trivalent oxidation state (commonly denoted RE^{3+}) is very frequently found for lanthanide ions

rare-earth ions are promising candidates for quantum memory applications.

Element Name	Atomic Number	Electron Configuration (RE ³⁺)
Lanthanum (La)	57	[Xe] 4f ⁰
Cerium (Ce)	58	[Xe] 4f ¹
Praseodymium (Pr)	59	[Xe] 4f ²
Neodymium (Nd)	60	[Xe] 4f ³
Promethium (Pm)	61	[Xe] 4f ⁴
Samarium (Sm)	62	[Xe] 4f ⁵
Europium (Eu)	63	[Xe] 4f ⁶
Gadolinium (Gd)	64	[Xe] 4f ⁷
Terbium (Tb)	65	[Xe] 4f ⁸
Dysprosium (Dy)	66	[Xe] 4f ⁹
Holmium (Ho)	67	[Xe] 4f ¹⁰
Erbium (Er)	68	[Xe] 4f ¹¹
Thulium (Tm)	69	[Xe] 4f ¹²
Ytterbium (Yb)	70	[Xe] 4f ¹³
Lutetium (Lu)	71	[Xe] 4f ¹⁴

Table 2.1: Lanthanides, the atomic number, and the electron configuration of their trivalent ion form

This thesis specifically focuses on erbium, which has an atomic number of 68 and 11 electrons in its 4f subshell. In the following section we will dive deeper into erbium, its properties, and its dynamics when doped into crystals.

2.2 Erbium Dopants in Calcium Tungstate

2.2.1 Host Crystal: CaWO₄

To begin with, the host crystal used for erbium dopants in this study, namely CaWO₄ will be introduced. Based on literature, the lattice constants of a CaWO₄ unit cell are $a = b = 0.524$ nm and $c = 1.138$ nm, resulting in a unit cell volume of approximately $V = 310 \text{ \AA}^3$ [13]. Figure 2.1 provides an illustration of a unit cell of CaWO₄. Structurally, CaWO₄ is a tetragonal crystal system within the I4₁/a space group. Upon doping with erbium ions, the site that the dopant occupies has an S4 point group symmetry, and

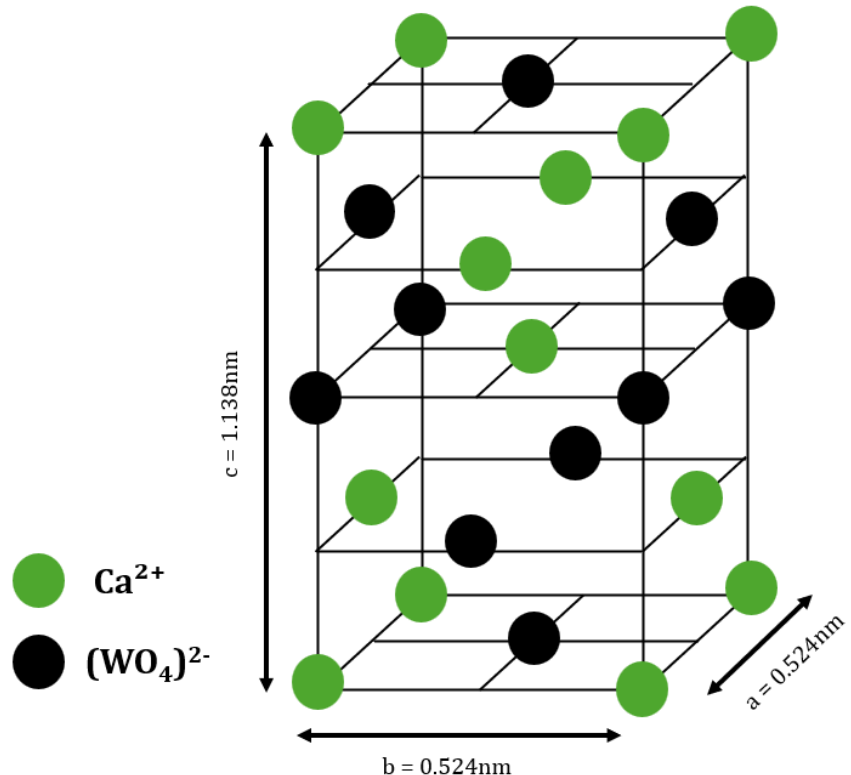


Figure 2.1: An illustration of the unit cell of calcium tungstate. Green circles represent calcium ions, and black circles represent an orthotungstate ion, which is the simplest tungstate ion. Upon doping with erbium, Er³⁺ ions will take the place of Ca²⁺

this local S4 symmetry is the cause of the loss of spherical symmetry that a free erbium ion would normally have, which is important in the following discussion regarding the energy level structure of erbium doped in calcium tungstate.

2.2.2 Energy Structure of Erbium

An overview of the energy structure of ¹⁶⁷Er embedded in a CaWO₄ crystal under the influence of magnetic fields is described in Figure 2.2. We shall now delve into the physical principles underlying this energy structure by discussing the Hamiltonian.

The total Hamiltonian of rare-earth ions comprises three primary terms: the free ion term, the crystal field term, and the spin Hamiltonian.

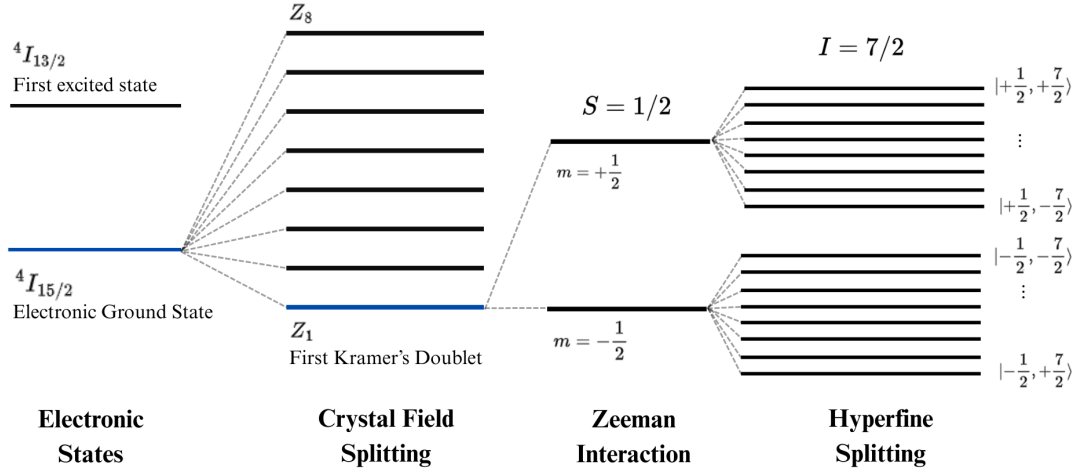


Figure 2.2: Energy Structure of ^{167}Er showing the splitting of the lowest energy levels (marked in blue) due to different interactions

$$\hat{H}_{\text{total}} = \underbrace{\hat{H}_{FI}}_{\text{Free Ion Energy}} + \underbrace{\hat{H}_{CF}}_{\text{Crystal Field Term}} + \underbrace{\hat{H}_{Spin}}_{\text{Spin Hamiltonian}} \quad (2.1)$$

Free Ion Hamiltonian

Firstly, we will briefly discuss the free-ion term. As the name suggests, the free ion term describes the rare-earth ion without the influence of any external fields. The free-ion Hamiltonian is affected by the ion's total potential and kinetic energy, the Coulomb interaction, and the coupling between the spin and orbital angular momentum (spin-orbit coupling). The spin-orbit coupling here is especially interesting, as it causes the system to split into energy levels corresponding to $J = S + L$, with L and S being the orbital and spin angular momentum. The energy levels are usually described using the Russell-Saunders notation $^{2S+1}L_J$ [13].

Using the Russell-Saunders notation, the ground state of free erbium ions can be labeled as $^4I_{15/2}$, and the first excited state is $^4I_{13/2}$. The transition between the electronic ground state and the first excited state is the optical transition of $1.5\mu\text{m}$, one of Erbium's properties widely used in optical fibers.

Crystal Field Hamiltonian

We will now briefly discuss the crystal field term. This term arises when the spin system is embedded into a crystal. Thus, the crystal field will break the spherical symmetry of the electronic structure from the free-ion Hamiltonian and split the ground state into further levels. Furthermore, Kramer's theorem states that if the number of electrons in the 4f shell is odd, then the crystal field levels will be doubly degenerate. The ground state of erbium will thus split into eight doubly degenerate Kramers doublets, each denoted as $Z_1 \dots Z_8$. In the special case of the system being in sub-Kelvin temperatures, only the lowest Kramer's doublet Z_1 is populated [13, 20].

Effective Spin Hamiltonian

The spin system's effective spin Hamiltonian consists of the Electron Zeeman term, the Hyperfine interaction Term, and the Nuclear Quadrupole Term.

$$\hat{H}_{\text{spin}} = \underbrace{g\mu_B \mathbf{B} \cdot \hat{\mathbf{S}}}_{\text{Electron Zeeman}} + \underbrace{\hat{\mathbf{S}} \cdot \mathbf{A} \cdot \hat{\mathbf{I}}}_{\text{Hyperfine}} + \underbrace{\hat{\mathbf{I}} \cdot \mathbf{Q} \cdot \hat{\mathbf{I}}}_{\text{Nuclear Quadrupole}} \quad (2.2)$$

At the ground state, the first Kramers doublet is doubly degenerate. Due to the Zeeman effect, under the influence of an external magnetic field B_0 , this degeneracy will be lifted, and the spin states of the effective spin 1/2 system will split into two as a result of the electron-Zeeman interaction, which is given by

$$\hat{H}_{EZ} = g\mu_B \mathbf{B} \cdot \hat{\mathbf{S}} \quad (2.3)$$

Where μ_B is the Bohr Magneton, B is the applied external magnetic field, and g is the Landé g -factor. For a spin system with zero nuclear spin, the electron Zeeman effect provides the resonance condition for the spin transition. However, in the case of the ^{167}Er isotope, which possesses a nuclear spin of $I = 7/2$, hyperfine interactions occur from the coupling between the electron and nuclear spin. Thus a splitting into $(2I + 1)(2S + 1) = 16$ energy levels takes place. The hyperfine interaction is generally given by

$$\hat{H}_{\text{Hyperfine}} = \hat{\mathbf{S}} \cdot \mathbf{A} \cdot \hat{\mathbf{I}} \quad (2.4)$$

With $\hat{\mathbf{S}}$ denoting the electron spin operator, A denoting the hyperfine tensor, and $\hat{\mathbf{I}}$ the nuclear spin operator.

Alongside the Zeeman and hyperfine interactions, one has to consider the nuclear

quadrupole effect. The nuclear quadrupole interaction plays a role in case the system has a nuclear spin number $I \geq 1$ [13]. In principle, uneven distribution of electric charges along the nucleus will cause an electric field gradient in its vicinity, and the interaction between the quadrupole moment of the nuclei with this gradient gives rise to the nuclear quadrupole interaction term in the spin Hamiltonian. [18]

In the spin Hamiltonian, the nuclear quadrupole interaction is given by the following term.

$$\hat{H}_{\text{NQI}} = \hat{\mathbf{I}} \cdot \mathbf{Q} \cdot \hat{\mathbf{I}} \quad (2.5)$$

Where \mathbf{I} is the nuclear spin, and \mathbf{Q} is the nuclear quadrupole tensor.

Based on [13], the known spin Hamiltonian parameters of Er with zero nuclear spin and its ^{167}Er isotope are summarised in 2.2.

Isotope	Electron Spin	Nuclear Spin	g_{\parallel}	g_{\perp}	A_{\parallel}/h (MHz)	A_{\perp}/h (MHz)
Er	1/2	0	1.247	8.38	0	0
^{167}Er	1/2	7/2	1.247	8.38	-130	-873

Table 2.2: Spin Hamiltonian Parameters of Erbium in Calcium Tungstate summarised.

The table displays the values of the g and A tensors with parallel and perpendicularly aligned magnetic fields. For the isotope with zero nuclear spins, no hyperfine interaction will take place, and thus, the value of the A tensor is 0.

2.3 Spin Dynamics

2.3.1 Two Level Quantum Systems and the Bloch Sphere

The quantum state of any arbitrary two-level quantum system can be represented as a superposition of the ground state and the excited state.

$$|\psi\rangle = \alpha|0\rangle + \beta|1\rangle \quad (2.6)$$

Coefficients α and β represent the probabilities and must follow the normalization condition.

$$|\alpha|^2 + |\beta|^2 = 1 \quad (2.7)$$

A Kramers doublet can be treated, and its dynamics can be analyzed as an effective spin $S = 1/2$ system. The dynamics of a two-level spin system are commonly visualized

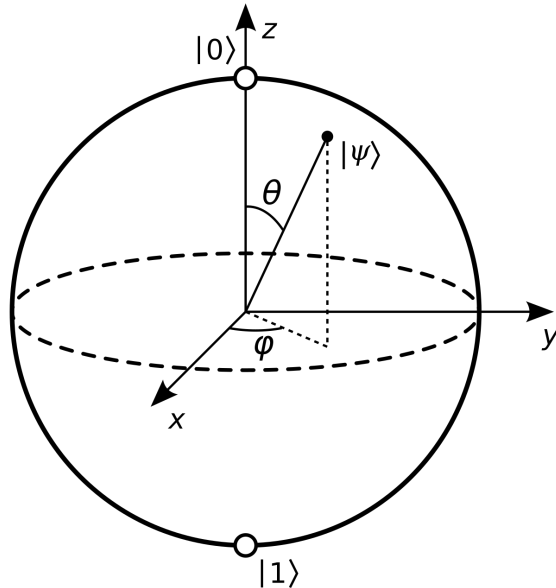


Figure 2.3: Bloch Sphere

using a Bloch sphere, which gives a geometric representation of a general two-level quantum system. The poles of the Bloch sphere on the z-axis represent the ground and excited states, denoted respectively using ket vectors $|0\rangle$ and $|1\rangle$.

Any arbitrary vector from the origin to any point on the surface of the Bloch sphere is, therefore, a superposition of the ground state $|0\rangle$ and the excited state $|1\rangle$. The states on the Bloch sphere are further characterized by their polar angle $0 \leq \theta \leq \pi$ and their azimuthal angle $0 \leq \varphi \leq 2\pi$. Therefore, a generalized spin state in the Bloch sphere can be summarised as a state vector.

$$|\psi\rangle = \cos \theta |0\rangle + \sin \theta e^{i\varphi} |1\rangle \quad (2.8)$$

2.3.2 Spin Relaxation Processes

Relaxation processes describe the energy exchange with a bath when out of thermal equilibrium. Based on the Bloch-Redfield Model, relaxation processes are described using two rates. The first is the longitudinal relaxation rate, also called the spin-lattice relaxation, which describes the decay of the excited state towards thermal equilibrium.

$$R_1 = \frac{1}{T_1} \quad (2.9)$$

T_1 relaxation can be visualized in the Bloch sphere as a longitudinal return of the state vector to the north pole of the sphere (ground state) after being excited by an external energy source.

The second one is transverse relaxation (T_2), also called spin-spin relaxation or spin coherence time, which describes the decay of the transversal components of the state vector in the Bloch sphere. Transverse relaxation is also related to longitudinal relaxation by adding the pure dephasing rate Γ_φ [12].

$$R_2 = \frac{1}{T_2} = \frac{R_1}{2} + \Gamma_\varphi \quad (2.10)$$

One can infer from this equation that an upper limit exists to spin coherence time with respect to the longitudinal relaxation time given by $T_2 \leq 2T_1$. Therefore, a long spin-lattice relaxation time is necessary for a higher achievable spin coherence time and is thus an important metric in quantum information technologies [4].

Spin Lattice Relaxation (SLR)

We will now emphasize the more detailed discussion of the spin-lattice (T_1) relaxation, which is the primary concern of this thesis, specifically the T_1 relaxation of the Er:CaWO₄ sample.

In principle, spin-lattice relaxation (SLR) describes the rate at which an electron spin returns to thermal equilibrium after being perturbed. The perturbation of a spin system by external energy sources will move it away from its thermal equilibrium. Interaction between the spin ensemble and its environment, in this case, interaction with the lattice of the host crystal CaWO₄, will induce energy loss within the spin system. The energy loss will then cause the longitudinal component of the state vector to return to the ground state over time, i.e., the population distribution of spin states at the system's energy levels returns to its original Boltzmann distribution at the state of thermal equilibrium. The relaxation follows a longitudinal decay function in the form of an exponential decay $A \cdot \exp(-\frac{t}{T_1})$. In complex systems with multiple energy levels, the decay is modeled in the form of a multi-exponential function $\sum_i A_i \cdot \exp(-\frac{t}{\tau_i})$.

The main processes involved in the SLR rate are the direct, Raman, and Orbach processes. The direct phonon process involves the exchange of phonons from the lattice to the spin system, whereas the Raman and Orbach processes are two-phonon processes [16]. Previous studies have shown that multi-phonon processes, i.e., Raman and Orbach processes, are negligible at sub-kelvin temperatures. Therefore, SLR in crystals at sub-kelvin temperatures is determined mainly by the direct exchange of phonons with the crystal lattice [4, 13]. Excluding the contribution from Raman and

Orbach Processes, the SLR rate is given by the following equation:

$$R_1 = \alpha_D(\vartheta)g^3(\vartheta)(\mu_B B)^5 \coth\left(\frac{\Delta E(\vartheta)}{2k_B T}\right) \quad (2.11)$$

where α_D is the coupling parameter for the direct phonon process. Here, angular dependency is considered, and thus, the coupling parameter α_D , the g factor, and the energy difference ΔE are dependent on the angle of the magnetic field ϑ .

Spin flip-flop interactions

One other relaxation mechanism between hyperfine levels in rare-earth-doped crystals is the so-called spin flip-flop interaction. In contrast to the direct process, which involves the exchange of phonons with the lattice, the flip-flop interaction is caused by the interaction between magnetic dipoles of two spins, inducing cross-relaxation if the two spins are spatially close together [6]. The flip-flop rate is given by:

$$R_{FF} = \beta_{FF}(\vartheta)n^2\Gamma \operatorname{sech}^2\left(\frac{\Delta E(\vartheta)}{2k_B T}\right) \quad (2.12)$$

where β_{FF} is the flip-flop coupling rate, n is the concentration of dopants, and Γ the inhomogeneous spin linewidth.

Magnetic field dependency of the SLR rate in rare-earth doped crystals has been shown by [4]. In this paper, the inhomogeneous linewidth is modeled based on its field dependency, resulting in the following equation.

$$R_{FF} = \frac{\gamma_{FF}(\vartheta)}{B} \operatorname{sech}^2\left(\frac{\Delta E(\vartheta)}{2k_B T}\right) \quad (2.13)$$

where γ_{FF} denotes the effective flip-flop coupling rate. Note that in equations 2.11-2.13, the magnetic field's angular dependency is considered. However, since the experiment in this work is carried out at a fixed magnetic field angle, we can remove the angular dependency from the picture. Therefore, the coupling rates are constant.

The strength of the magnetic field also plays a role in determining the overall relaxation rate. At low fields, the flip-flop process dominates the relaxation rate. However, as the magnetic field increases, the direct process will overpower the flip-flop process.

CHAPTER 3

Experimental Methodology

3.1 Broadband Electron Paramagnetic Resonance Spectroscopy with Superconducting Coplanar Waveguides

The main experimental method used in this work is broadband electron paramagnetic resonance (EPR) spectroscopy.

Broadband electron paramagnetic resonance spectroscopy is a frequently used technique for characterising the magnetic properties of electronic spins in solids. This technique utilises the magnetic moment from the spin of unpaired electrons. In the presence of an external magnetic field, the degeneracy of the spin states will be lifted due to the Zeeman effect, and the energy difference between the states will linearly increase as a function of field. When an electromagnetic wave propagates into the system that fulfils the resonance condition, i.e. the frequency of the incident wave is equal to the energy difference between the spin states, a transition will occur. Energy from the propagating microwave will be absorbed by the spin system at its resonance frequency. This specific frequency is referred to as the spin transition frequency.

The standard method for Broadband electron paramagnetic resonance involves coupling the spin system to a microwave cavity or a resonator. A microwave signal is then applied, and the transmission/absorption of the signal under the influence of an external magnetic field is measured. However, this method is limited to a narrowband frequency range. Various studies have thus been done to develop techniques allowing broadband measurements.

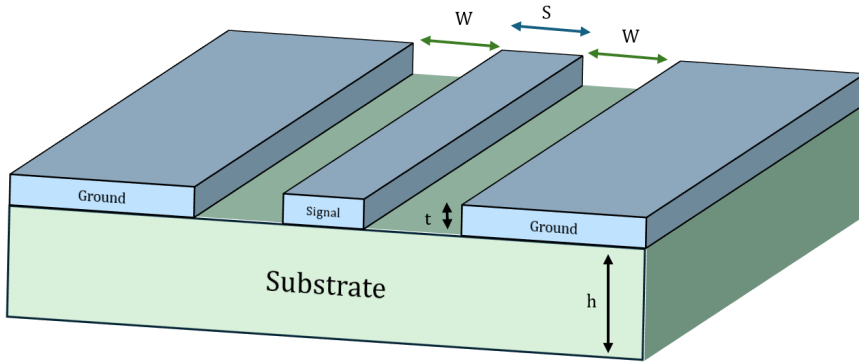


Figure 3.1: Basic illustration of a coplanar waveguide. Two ground conductors are separated from the signal line by a gap denoted by W . Both the signal and ground conductor planes are fabricated directly on top of a dielectric substrate of thickness h

Developments in recent years have provided a novel technique utilising superconducting coplanar waveguides that allows broadband measurements in Broadband electron paramagnetic resonance experiments [3, 11, 20]. For example, Clauss et al. [3] have demonstrated the use of such superconducting coplanar waveguides for the characterisation of rare-earth spin systems, namely Cr^{3+} ions embedded in ruby at cryogenic temperatures, where the coplanar waveguide is superconducting. In the following section, the working principle of superconducting coplanar waveguides will be briefly discussed.

Superconducting Coplanar Waveguides

In microwave engineering, waveguides are transmission line structures used to guide electromagnetic waves in a certain propagation direction by restricting the transmission of energy to one direction only. Various structures are used for waveguides, such as rectangular waveguides, microstrip waveguides, planar waveguides, a coaxial cable, or a coplanar waveguide. The coplanar waveguide (CPW) is especially interesting as it is relatively simple to fabricate. Furthermore, it has had many applications in quantum optics and quantum information processing [7].

A coplanar waveguide is a transmission line structure for microwaves that consists of a dielectric substrate, a central conductor strip, and two ground conductor planes. The ground planes and the center strip are both placed on top of the dielectric substrate, which has a thickness h and are separated by a gap w . The central conductor strip functions as the signal line for the microwave to propagate, and the ground planes for

the return current. Figure 3.1 illustrates a coplanar waveguide.

Electromagnetic waves propagate through a coplanar waveguide in a quasi-TEM (Transverse Electromagnetic) mode. In standard TEM modes, the electric and magnetic fields are completely transverse to the wave vector, whereas in a quasi-TEM mode, small longitudinal components exist due to the inhomogeneous environment of the waveguide [19].

3.2 Measurement Setup

The main components of the experimental setup used in this work consist of a helium dilution refrigerator¹, a vector network analyser², a coil to generate magnetic fields to study the field dependency of the system, and the spin system itself. The spin system consists of an Er:CaWO₄ sample coupled to the transmission line, which is a superconducting coplanar waveguide. The doped crystal has a size of $0.6 \times 8 \times 9 \text{ mm}^3$ ($a \times b \times c$) and is placed on top of the coplanar waveguide. The spin system will be located at the cryostat's mixing chamber stage, which can cool down below 7 mK. The coil's static magnetic field (B_0) is oriented parallel to the microwave propagation vector (k) and perpendicular to the crystal c-axis.

$$B_0 \parallel k \perp c$$

Microwaves from the 1st port of the VNA propagate towards the spin system using coaxial cables. The input microwave signal is attenuated by -20 dB before entering the cryostat, and within the various stages of the cryostat, the signal is further attenuated by -29 dB. On the output side, the signal is first fed into a circulator which has a 50Ω resistor on the 3rd port. The signal is then amplified using a High-Electron-Mobility-Transistor (HEMT) at the 4K stage of the cryostat, and then further amplified in room temperature before the signal is fed into the 2nd port of the VNA. This is schematically shown in Figure 3.2.

The system will be characterised by measuring its properties using a Vector Network Analyser, whose working principle will be discussed briefly in the following section.

VNA Measurements

A Vector Network Analyzer (VNA) is an instrument commonly used in Radio Frequency (RF) and microwave engineering. It can transmit microwave electromagnetic signals to the device under test (DUT) and measure the amplitude and phase of the response. The

¹Bluefors LD-400

²Rohde und Schwarz ZNA

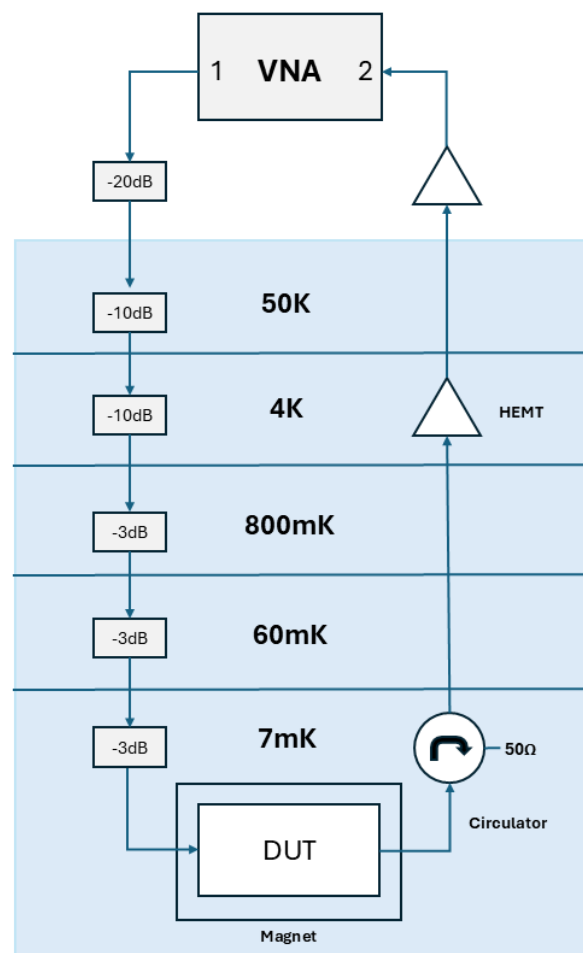


Figure 3.2: Measurement Setup

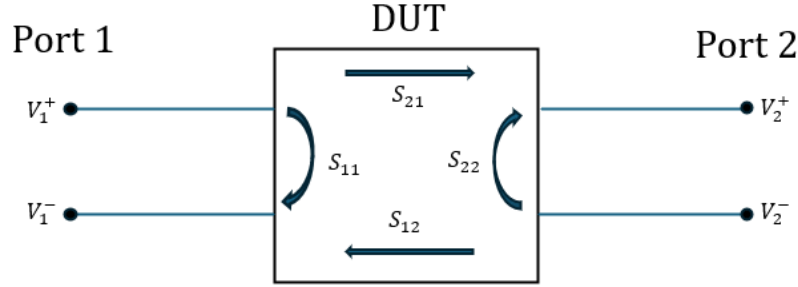


Figure 3.3: Two Port VNA and S-Parameters

response can be measured in the form of the reflected and transmitted signal, which are called scattering parameters or *S*-parameters. In general, *S*-parameters indicate the ratio between the voltage transmitted and reflected.

$$S_{mn} = \left. \frac{V_m^-}{V_n^+} \right|_{V_{r\neq n}^+=0} \quad (3.1)$$

For the case of a two-port VNA, there are four *S*-parameters, denoted S_{11} , S_{12} , S_{21} , S_{22} . The S_{11} and S_{22} parameters are input and output reflection parameters, whereas S_{12} and S_{21} are reverse and forward transmission parameters. Figure 3.3 illustrates a two-port VNA and the scattering parameters.

In a two-port network, the relation between *S*-parameters with the incident (V_1^+ , V_2^+) and reflected voltages (V_1^- , V_2^-) can be summarized in the following matrix vector notation.

$$\begin{bmatrix} V_1^- \\ V_2^- \end{bmatrix} = \begin{bmatrix} S_{11} & S_{12} \\ S_{21} & S_{22} \end{bmatrix} \begin{bmatrix} V_1^+ \\ V_2^+ \end{bmatrix} \quad (3.2)$$

For the spin-resonance experiment in this thesis, measurement of the complex forward transmission, namely the S_{21} parameter, is of primary concern. In principle, the S_{21} is measured as a function of frequency. When the spin system absorbs energy from the input microwave signal at its resonance frequency, we can observe a dip in the S_{21} parameter, which corresponds to the lineshape curve of the spin transition at this specific resonance frequency.

3.3 T_1 Measurement via Saturation Recovery

The Spin-Lattice Relaxation (T_1) time of this system is determined by direct microwave absorption of spin transitions measured using the saturation recovery method. The principle of saturation recovery is described in this section. In ESR experiments on spin ensemble systems, the microwave power from the VNA fundamentally alters the system's energy absorption characteristics. Low microwave powers are used to probe the spin transitions, as the absorption signal of low powers directly reflects the population difference between the energy levels [16]. On the contrary, when high microwave powers are pumped into the system, the spin ensemble will saturate. This means that the population difference between energy levels will be reduced, and thus, the absorption signal will become weaker. Visually, this saturation can be seen as a progressive decrease in the absorption dip depths.

For this specific sample (Er:CaWO₄), the maximum microwave power that can be used to probe the system without saturating the spins lies at -42 dBm. This probe power was determined by sweeping the microwave power at the transition frequency and observing at which input power saturation begins to happen. Figure 3.4 shows a progressive sweep of input powers from the VNA on the 2.7 GHz transition, starting from -60 dBm up to -10 dBm. As mentioned before, saturation can be observed visually as a progressive shallowing of the dip's depth, which one can observe in the figure as input powers increase. On the highest input power (-10 dBm), we can observe that the transmission is almost flat, implying that the system is almost entirely saturated. When the spin system is fully saturated, the population difference is eliminated, and no energy absorption can be observed in the transmission signal, resulting in a flat line.

In the saturation recovery experiment, rounds of high microwave power are pumped to saturate the spin transition by sweeping the VNA frequency across a narrow frequency window containing the spin transition. After the pumping process is stopped, the system will slowly relax back to its thermal equilibrium state, where the Boltzmann distribution governs the population distribution. This relaxation process is monitored by probing the S_{21} parameter at low probing power over time. The spin ensemble will return to its equilibrium state following a multi-exponential relaxation pattern with the T_1 times as the parameter of the exponential decay function.

In this thesis, the following routine was established for the saturation recovery experiment. First, we defined the key measurement parameters, including the desired field strengths, center frequency, frequency span, spectroscopy resolution, duration of decay measurements, temporal resolution, and intermediate frequency bandwidth (IFBW) of the VNA.

Once these parameters were set, the magnetic field was ramped up to the desired strength. After reaching the targeted field, the pumping phase began. During this stage,

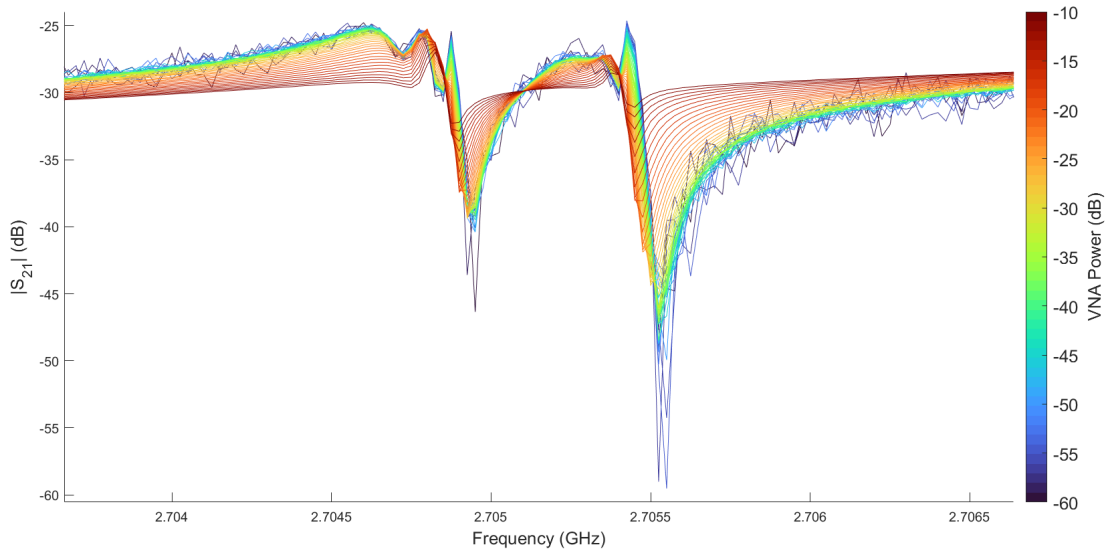


Figure 3.4: Microwave powers from the VNA are swept from -60 dB to -10 dB at the 2.7 GHz transition in Zero-Field conditions. The maximum power that can be used to probe the spin transition without saturating it is -42 dB.

20 cycles of high microwave power (-5 dB) were applied to saturate the spin system. After saturating the spin system, the microwave input was lowered to a power of -42 dB to probe relaxation without further saturating the spin ensemble. This part of the measurement will be referred to as decay probing. Once the spin ensemble had fully relaxed, the magnetic field was increased, and the measurement cycle was repeated. This entire process is illustrated schematically in Figure 3.5.

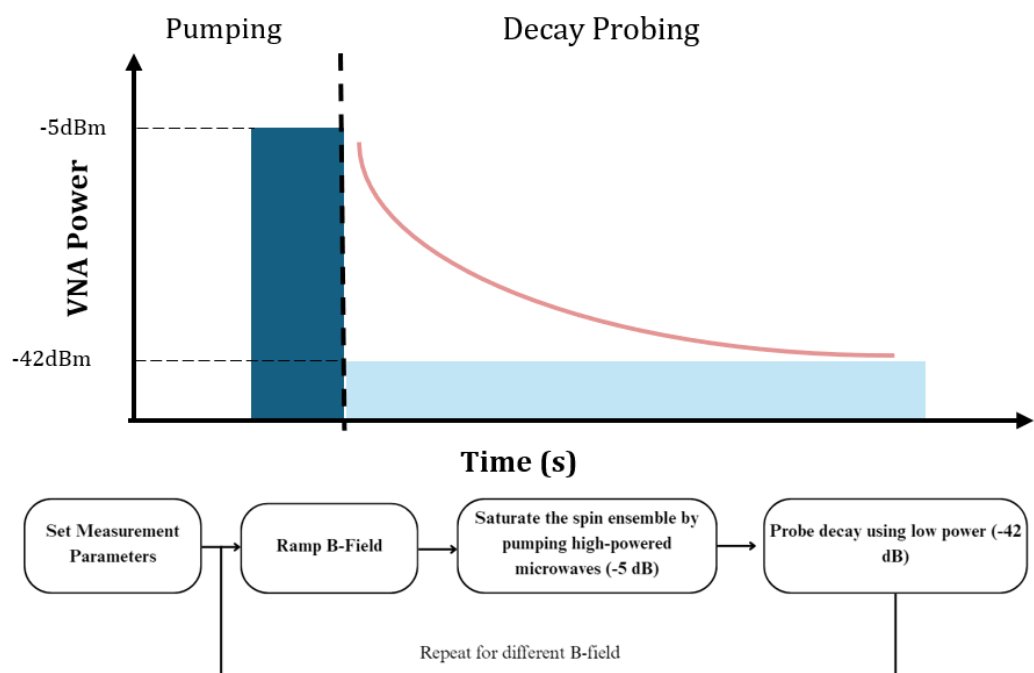


Figure 3.5: Saturation Recovery Measurement Cycle

CHAPTER 4

Results

4.1 Zero Magnetic Field Spectroscopy

In this section, we will present and discuss the results of spectroscopy conducted on hyperfine transitions under zero-field conditions. In these conditions, the energy level splitting is determined by the field-independent components of the effective spin Hamiltonian, specifically the hyperfine and quadrupole interactions [20]. It is important to note that in zero-field spectroscopy, the Zeeman interaction, which depends on the presence of a magnetic field, does not play a role. Only as the magnetic field strength increases will the Zeeman interaction begin to dominate.

To start with, a broadband spectroscopy of the sample from 0.1 to 4 GHz with an input power of -43 dBm at the VNA is shown in Figure 4.1. In the S_{21} subplot, background resonances that could be caused by various instrumentation and environmental factors can be seen as sharp dips which do not correspond to the spin transitions of the sample. To carefully study the spin transitions, further measurements with narrowband frequency spans will be shown.

Figure 4.2 presents spectroscopy results obtained at four different frequency spans: 2.65-2.658 GHz, 2.7-2.71 GHz, 3.18-3.19 GHz, and 3.48-3.49 GHz. All measurements were taken using a Vector Network Analyzer (VNA) power of -43 dB and an intermediate frequency bandwidth (IFBW) of 100 Hz. Assuming the probing VNA power of -43 dB is sufficiently low to avoid any saturation during the spectroscopy measurements, absorption dips can be observed in each frequency span, which correspond to the hyperfine transitions of the sample.

4 Results

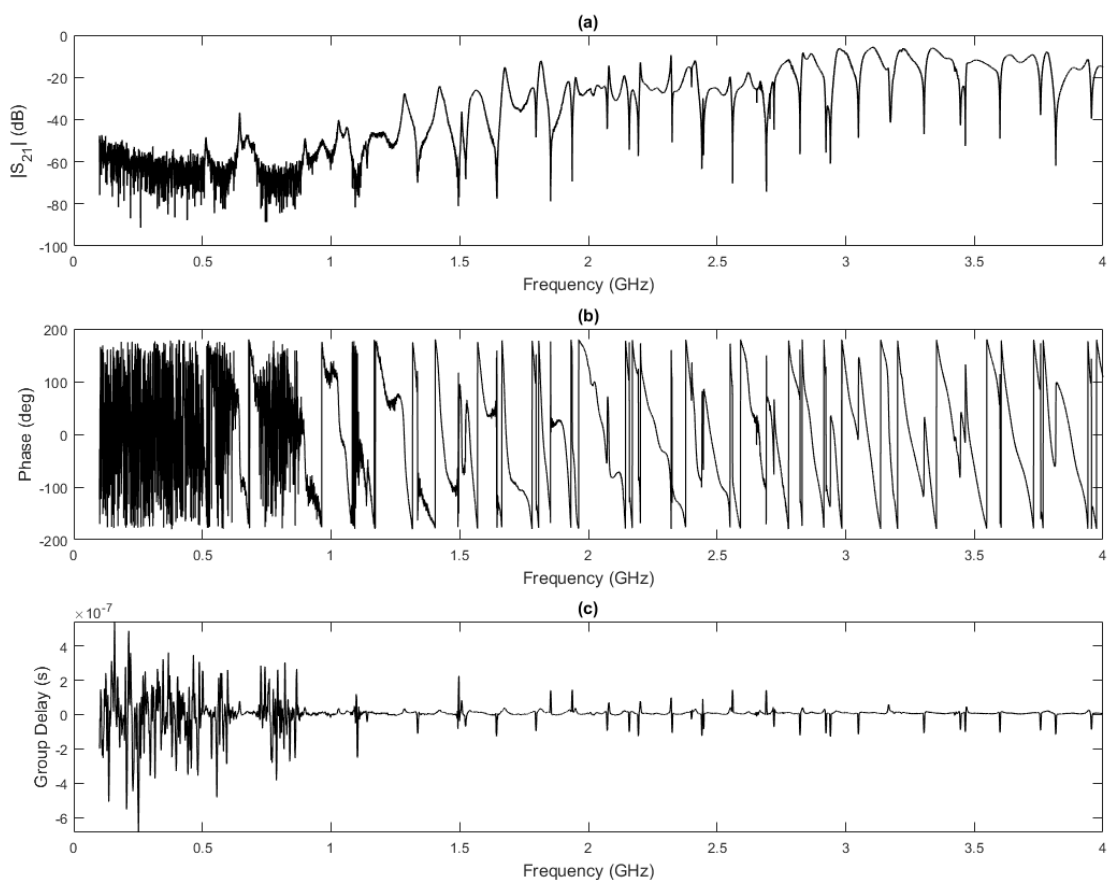


Figure 4.1: Broadband Spectroscopy of Er:CaWO₄ from 100 MHz to 4GHz. (a) Transmission coefficient S_{21} in decibels. (b) Phase shift in degrees. (c) Group delay measured as electrical delay.

4 Results

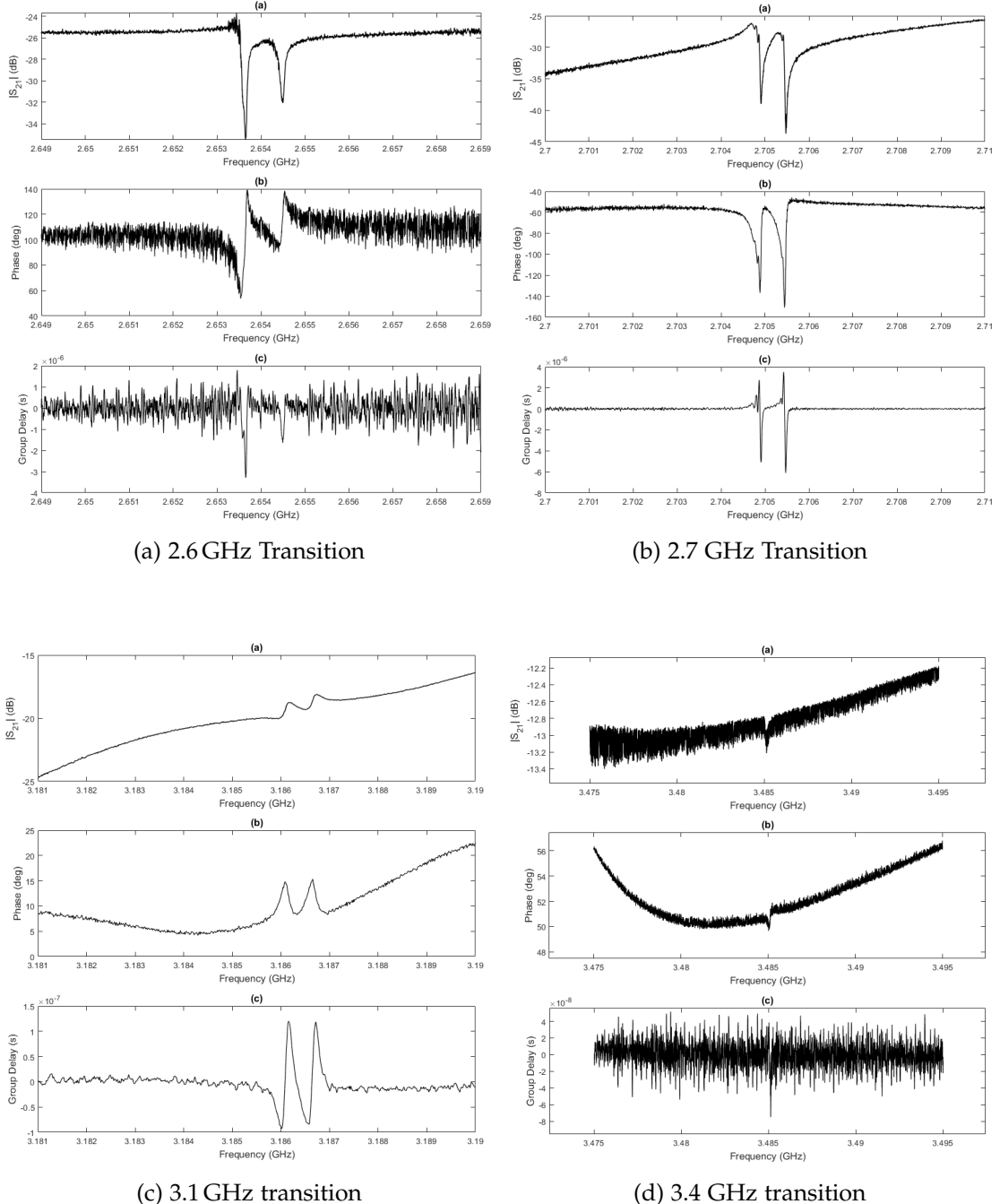


Figure 4.2: Zero-Field Spectroscopy of Hyperfine Transitions. $|S_{21}|$, phase and group delay of transitions detected at 2.654 GHz (a), 2.705 GHz (b), 3.185 GHz (c) and 3.485 GHz (d).

4.2 Magnetic Field Sweeps

Spectroscopy measurements under swept magnetic field values will now be presented. The magnetic fields are swept to observe how the transition frequencies change with the applied field. Through magnetic field sweeps, one can also observe how the Zeeman interaction will start to dominate at higher fields. Moreover, high-resolution field sweeps near zero field will reveal the offset in the applied magnetic field created by the power supply of the magnet, which is crucial for making corrections in the data analysis process. Normalization of the field sweeps is done by constructing a composite background in the spectrum where no energy absorption by the spin ensemble happens. This composite background is used in order to mitigate any artefacts in the $|S_{21}|$ that do not correspond to any spin transitions.

To begin with, a magnetic field sweep from -2 mT to 30 mT was conducted on the sample. This measurement is done with a field resolution of 0.5 mT and frequency resolution of 75 kHz over a span from 2.2 GHz to 2.8 GHz. The results are shown in Figure 4.3, which shows both the transmission (S_{21}) and the phase. Despite background resonances being visually present in the plots in the form of vertical lines, we can observe hyperfine transitions in the plot and its magnetic field dependence. The curves illustrate how the transition frequencies evolve with varying magnetic fields.

By sweeping the magnetic fields up to 30 mT, one should also be able to observe the Zeeman transition of the erbium isotopes with zero nuclear spin as a linear function. We can also observe that the Zeeman interaction starts to dominate over the hyperfine interaction as the magnetic fields get higher. A linear fit of the Zeeman transition results in the parameters summarized in table 4.1. Physically, we can interpret the p_2 parameter as an offset in the magnetic field. More interesting is the physical interpretation of the p_1 parameter, which is the slope between the magnetic field with respect to frequency. This parameter represents the inverse of the gyromagnetic ratio divided by 2π . Furthermore, the fitted p_1 parameter allows us to derive the g-factor, given by:

$$g = \frac{h}{p_1 \mu_B} \quad (4.1)$$

with h denoting Planck's constant and μ_B denoting Bohr's magneton. Inserting the known values of h and μ_B , we find a g-factor of 8.41, a value that is consistent with other measurements in literature.

In contrast to the low-resolution high-range sweep shown in Figure 4.3, the following Figure 4.4 shows a very high-resolution field sweep from -2 to 2 mT. In this measurement, the frequency resolution is 5 kHz and the field resolution is 0.01 mT. From this measurement, we can visually observe that the zero field shown in these measurements is not the true zero field. An offset of approximately 0.208 mT, which

4 Results

p_1 (mT/GHz)	p_2 (mT)
8.5583	0.2084

Table 4.1: Parameters from linear fitting of the Zeeman transition with the fitting function $f(x) = p_1x + p_2$.

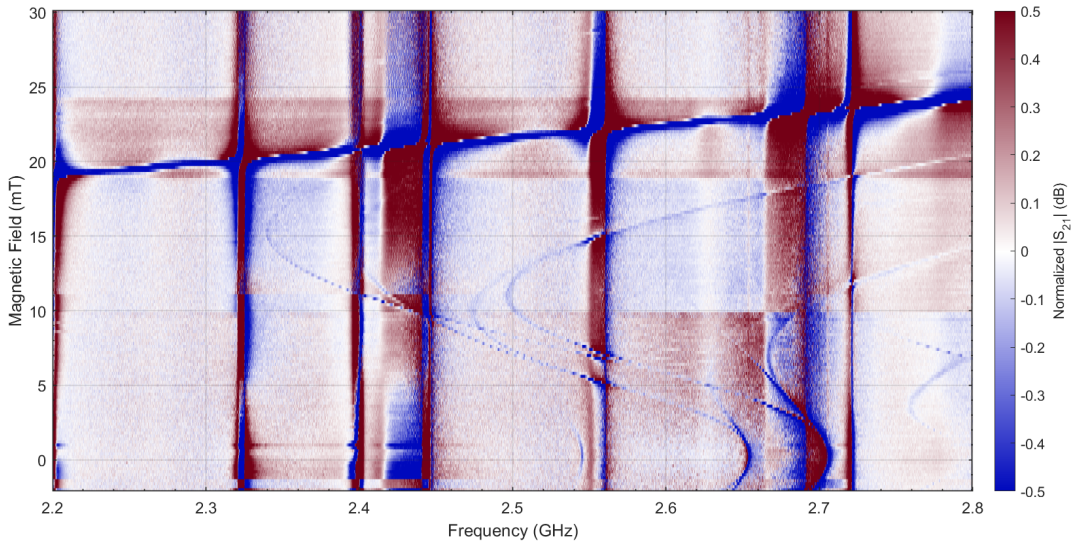


Figure 4.3: Normalized transmission and phase data from a magnetic field sweep from -2 to 30 mT.

was first established in the fitting of the Zeeman line, was visually confirmed in the high-resolution field sweep. A possible explanation for this offset is a leakage current in the power supply system, which feeds the magnet.

4.3 Spin-Lattice Relaxation Measurements

In this section, the results of the saturation recovery experiment are presented. We will first discuss the procedure used to analyze the data and look into zero field measurements. Afterwards, the results of the field-dependent measurements will be shown.

As discussed previously, the saturation recovery measurements consist of two important steps, pumping and decay probing. In all the following measurements, pumping was done with 20 high-power frequency sweeps with a power of -5 dB at the

4 Results

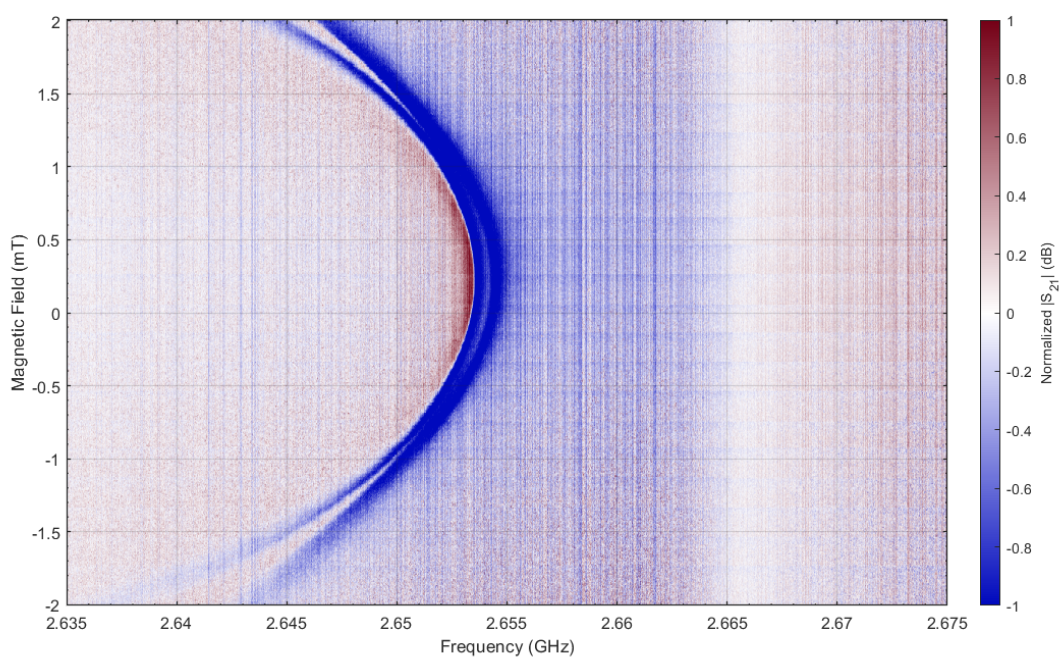


Figure 4.4: Near zero-field high resolution sweep.

VNA, and the decay probing was done using a VNA power of -42 dB.

4.3.1 Correction and Analysis Procedure

Circle Fitting Correction Procedure

Before delving into the analysis of microwave absorption data, it is important to consider the distortion in the data due to the microwave environment of the setup, such as effects from cable length and impedance mismatches, as well as miscalibrations in the various stages of the experiment. In order to correct this and also normalize the data, a routine based on analysis of the measured data in the complex plane was done based on Probst [15]. This paper presented a method to analyze noisy and complex scattering data on microwave resonators. This same method will be applied to this thesis.

The correction procedure involves fitting the microwave absorption data in the complex plane, where the data points of the Lorentzian lineshape appear as a circle. The background spectrum, which is ideally constant in transmission and phase, is located at a fixed point in the plane.

To normalize the data, the data points must be translated into the real axis and rotated such that the circle lies in their canonical position, i.e., the background should be located at 1 on the real axis. This is achieved by fitting the circles of the raw data and then using the fitted parameters to determine the translation and rotation values. Subsequently, magnitude and phase are recalculated from the corrected dataset.

As an example, Figure 4.5 shows the lineshape curves of the 2.6 GHz and 2.7 GHz transitions from zero-field spectroscopy measurements transformed into the complex space. The first row of the figure shows the original spectroscopy dataset, and the second row shows the corrected dataset. The circle fit correction procedure removes any asymmetry in the amplitude signal caused by the microwave environment. This procedure is then repeated on every single trace of the decay measurements. The result will be the decay data with a clean background that has a baseline transmission value of 1. Figure 4.6 shows the result of this correction procedure on the 2.6 GHz transition.

To extract the relaxation time from the decay measurements, the intensity of each trace will be analyzed and numerically integrated. The values of its integral will be plotted as a function of time, where we expect the curve to take the form of a multi-exponential function.

Lambert-Beer Analysis

Analysis of the absorption intensity is based on Lambert-Beer's law. The change in intensity of electromagnetic radiation (in this case, microwaves) is described by

4 Results

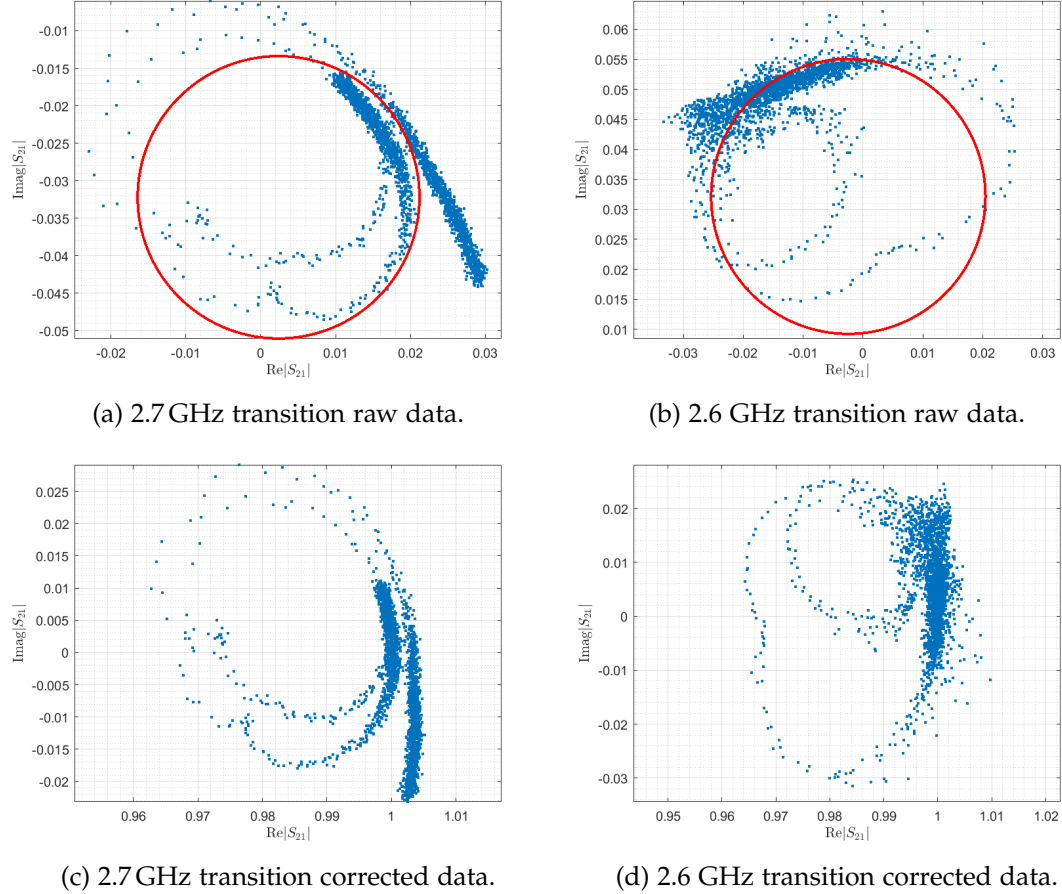


Figure 4.5: Complex-plane representation of the lineshape curves for the 2.6 GHz (right column) and 2.7 GHz (left column) spin transitions. Each absorption dip appears as a circle, and the background corresponds to the areas with a high density of data points. Figures (a) and (b) show the original measured data with their fitted circles, (c) and (d) show the complex data after applying the circle fit correction procedure.

4 Results

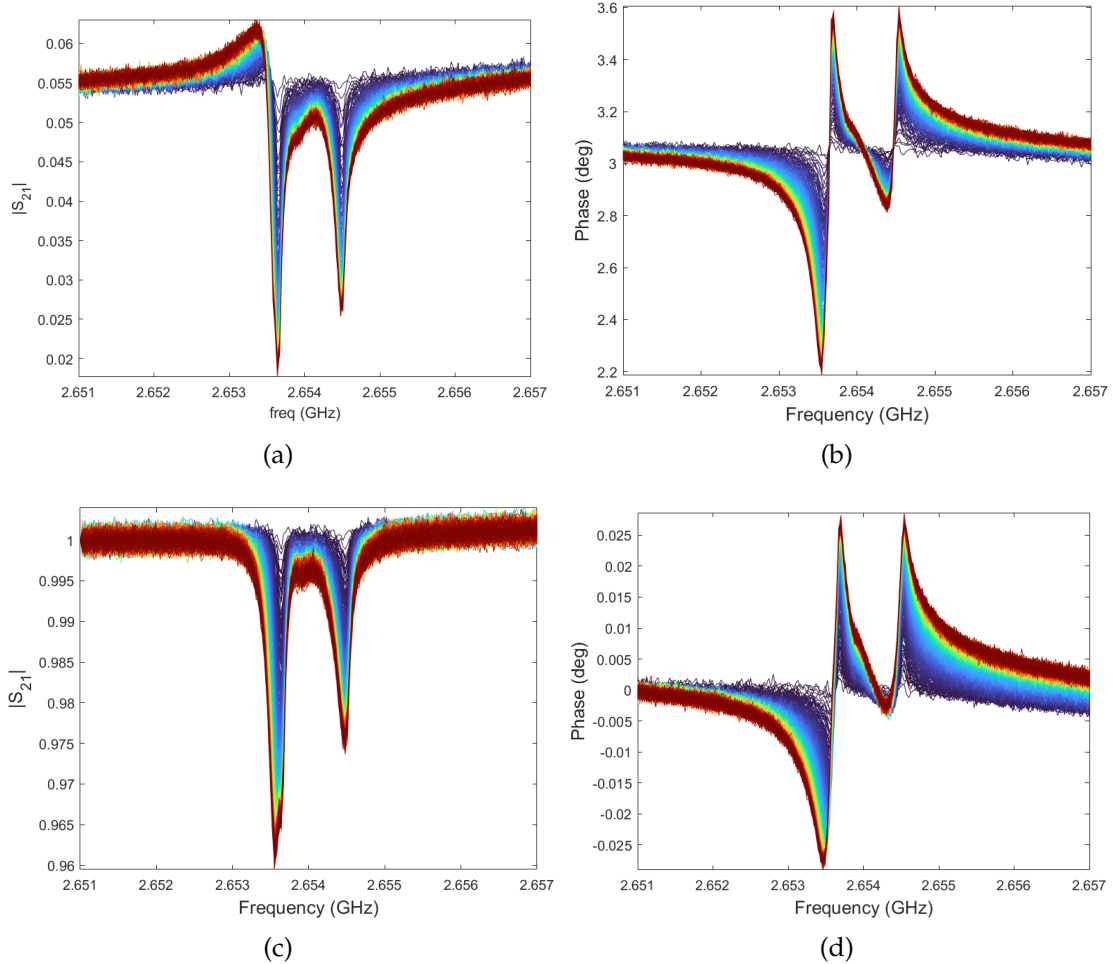


Figure 4.6: A comparison of the original transmission and phase data from direct measurement against the corrected and normalized data. (a) shows the S_{21} and (b) shows phase of the 2.6 GHz transition measured by the VNA. After applying the circle correction procedure, the resulting decay data has a flat background with a baseline transmission value of 1, shown in (c), and an initial background phase of 0 degrees, as shown in (d).

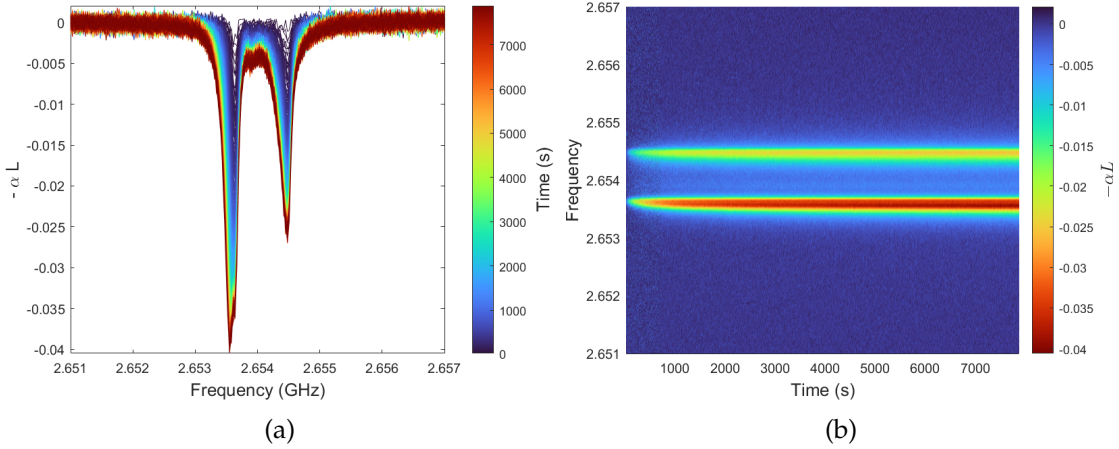


Figure 4.7: $-\alpha L$ coefficient of the 2.6 GHz transition in zero-field. (a) shows all $-\alpha L$ traces as a function of frequency, with the blue lines representing saturated traces and red lines representing the relaxed traces. (b) shows the time evolution of $-\alpha L$

Lambert-Beer's law. In its general form, the law can be described using an exponential function

$$I = I_0 \cdot e^{-\alpha L} \quad (4.2)$$

where I is the transmitted intensity after passing the sample, I_0 the incident intensity, α the absorption coefficient, and L denotes the path length through the material.

In this case, the background is treated as incident intensity, i.e. a fully saturated line. I_0 is constructed by fitting a linear function from the background data points without considering the ones from the absorption dip. After dividing each trace by the background and taking its natural logarithm, we are left with $-\alpha L$, which is a dimensionless quantity with a baseline of 0.

$$\ln\left(\frac{I}{I_0}\right) = -\alpha L \quad (4.3)$$

Figure 4.7 presents the $-\alpha L$ for the zero field decay data. In this specific measurement, the temporal resolution is 2696 traces over approximately 8000 seconds.

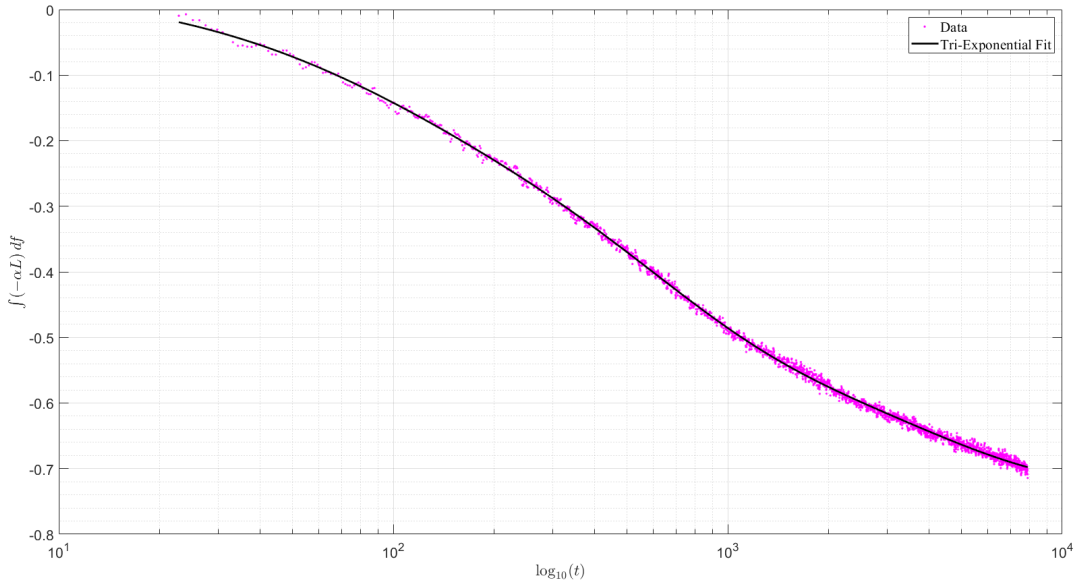


Figure 4.8: Integral of $-\alpha L$ as a function of logarithmically scaled time after the pumping sequence. Each data point corresponds to the numerically integrated value of a single $-\alpha L$ trace over frequency. A fitted tri-exponential curve is plotted over the calculated integrals (magenta dots) using a black line. The fitting results are summarized in Table 4.2

Multi-exponential Fitting

Numerically integrating each $-\alpha L$ trace will result in a multi-exponential decay trend over time. Figure 4.8 shows the integrated $-\alpha L$ spectra of the zero-field decay measurement from Figure 4.7. In the logarithmic time scale, we can see three different regions corresponding to a specific relaxation time, based on which the fitting is done using a tri-exponential function and an offset parameter d , which represents the absorption area when the system reaches thermal equilibrium. The fitted function represents the decay of the integrated areas as a function of time.

$$A(t) = a \cdot e^{-\frac{t}{\tau_1}} + b \cdot e^{-\frac{t}{\tau_2}} + c \cdot e^{-\frac{t}{\tau_3}} + d \quad (4.4)$$

The resulting extracted coefficients in zero-field conditions are summarized in Table 4.2. The tri-exponential function from these parameters is also plotted as a black line in Figure 4.8 over the integral values (magenta dots).

The observed tri-exponential relaxation pattern arises from the complex hyperfine

a	b	c	$\tau_1(s)$	$\tau_2(s)$	$\tau_3(s)$	d
0.2513	0.37464	0.14043	3544.1	494.78	67.609	-0.72838

Table 4.2: Decay Fitting Parameters

structure of the ^{167}Er isotope due to its nuclear spin of $I = 7/2$. This isotope exhibits a multi-level system with multiple decay channels; thus, the different relaxation times τ_1 , τ_2 , τ_3 . The amplitudes of each exponential component can be interpreted as the proportion of the spin population that relaxes through the corresponding decay channel. A larger amplitude means the specific relaxation process contributes higher to the overall relaxation behavior. In zero field, we observe amplitude b, which is associated with a relaxation time of $\tau_2 = 494.78\text{ s}$, being the largest among the three with a value of 0.37464. This implies that in zero field, most of the spin population relaxes within this relaxation time.

4.3.2 Field Dependent Measurements

Up to this point, we are mainly concerned with the relaxation in zero-field conditions. In this section, the aim is to observe how the T_1 relaxation time changes under the influence of low magnetic fields. This section will focus on the characterization of the 2.6 GHz transition and its spin-lattice relaxation in the presence of different magnetic fields. The 2.6 GHz transition was selected due to its relatively flat background, for which reason the best results from the circle plot correction routine are achieved at this transition.

Magnetic Field (mT)	0.3	0.55	0.8	1.05	1.3
Center Frequency (GHz)	2.65406	2.65362	2.6526	2.6513	2.6495

Table 4.3: Magnetic field vs. center frequency

Based on the field sweep measurements, a shift in the transition frequencies can be observed in the presence of a magnetic field. To compensate for this shift, the center frequency for each saturation recovery measurement is shifted accordingly for each field value. Table 4.3 shows the center frequencies used for measurements at different magnetic fields. The magnetic fields shown in this table are corrected for an offset of 0.2 mT. Every measurement is performed with an intermediate frequency bandwidth (IFBW) of 200 Hz, a resolution of 201 points, in a frequency span of 6 MHz.

Using the same approach as discussed in the previous section, we obtain the $-\alpha L$

data for the 2.6 GHz transition at each magnetic field, which is shown in Figure 4.9. Several observations can be made regarding the field dependency of the $-\alpha L$ coefficient. Firstly, the transition frequency shifts as expected based on the magnetic field sweeps done in section 4.2. This happens due to the Zeeman interaction, which starts to have an influence on the spin Hamiltonian as the magnetic field is introduced. However, in the low magnetic fields, the hyperfine interaction still dominates, and the magnetic field is treated simply as a perturbation, which explains why the change in center frequency is relatively small. Another observation to be made is that the absorption dips lose in peak absorption while broadening with the increasing magnetic field. In other words, we can observe a broadening of the hyperfine transition. Another possible explanation is the change of population distribution in the spin system with respect to the changing magnetic field. This explains why the relative intensities of different absorption components are affected as we change the magnetic field.

Plotting the fit parameters as a function of the magnetic field gives us Figure 4.10, which illustrates the magnetic field dependency of the spin-lattice relaxation of the sample in the low field regime, where we expect the direct flip-flop interaction to dominate the relaxation rate as discussed in section 2.3.2.

The tri-exponential fit provides us with three different time constant parameters τ_1 , τ_2 , and τ_3 , each denoting different spin-lattice relaxation components of the system. The values of the fastest relaxation component τ_3 lie between 8 and 30 seconds. The intermediate constant τ_2 represents the components relaxing with characteristic times in the range of 30 to 70 s. The time constant of spins that relaxes slowest is represented by τ_1 , which takes values of up to several hundred seconds. Based on τ_1 , which is the slowest relaxation component, we can see that generally under the influence of low magnetic fields, the longest component exhibits a characteristic relaxation time of around 500–600 s, indicating extended lifetimes of excited states of the Erbium sample.

The longest relaxation time τ_1 is weighted by the amplitude parameter a , whose value decreases as the magnetic field increases, as seen in Figure 4.10. In contrast to this trend, the values of the b and c amplitudes remain relatively constant or even slightly increase as the magnetic field strength is increased. Amplitude c , which corresponds to the fastest time component τ_3 has a low value initially in zero field. However, it dominates the relaxation at higher fields, for example at 0.8 mT where its weight overpowers that of the a and b components, indicating a very fast relaxation process for a majority of the spin ensemble. This indicates that as the magnetic field increases, the spin population will mostly relax quickly. In spite of this trend, the amplitude corresponding to the time constant τ_1 still makes a contribution to the overall relaxation trend in the higher fields, which indicates that the slow relaxation processes are still active and the spin system would still need a few hundred seconds in order to fully relax to its thermal equilibrium state.

4 Results

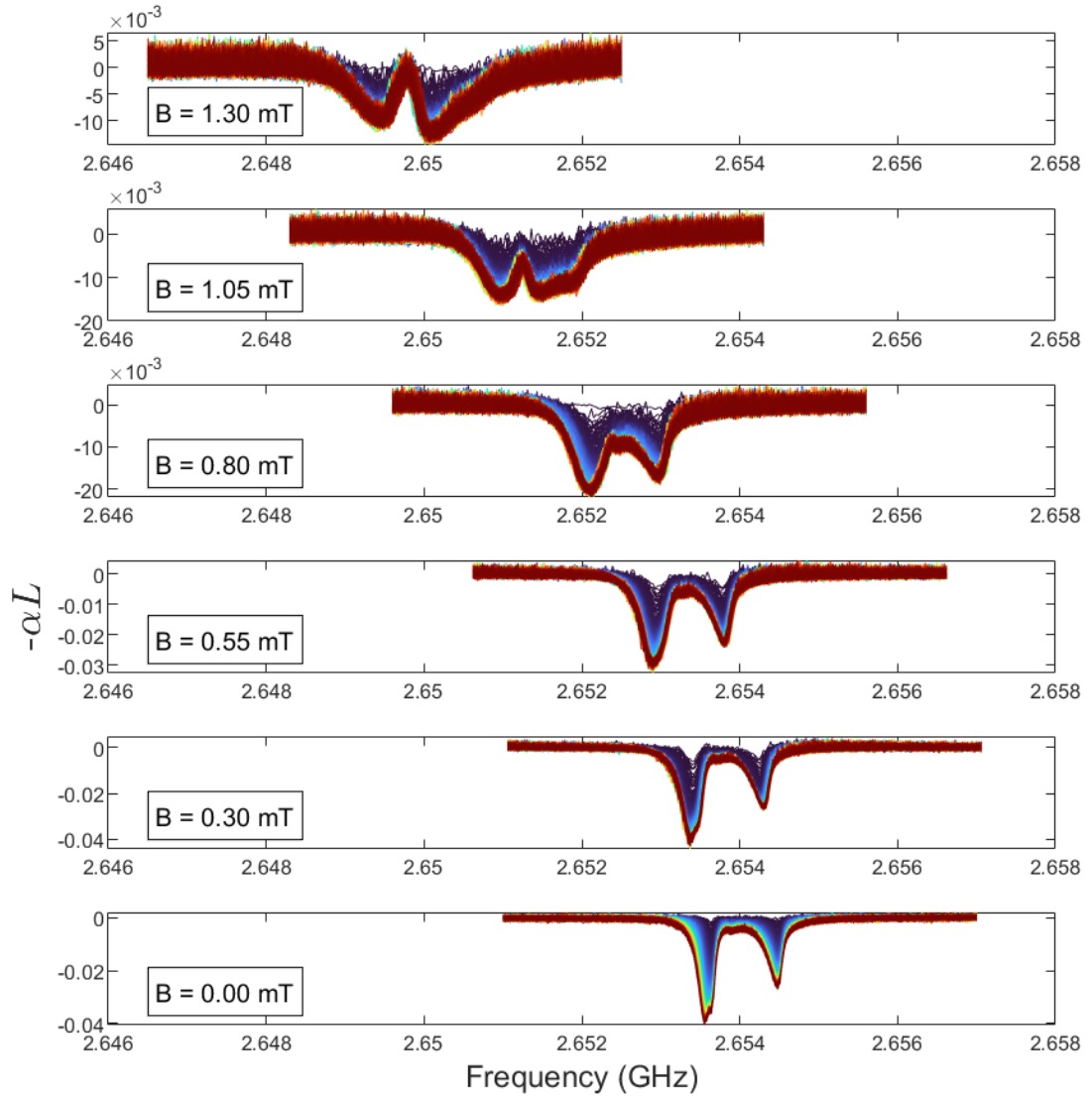


Figure 4.9: αL of the decay measurement at the 2.6 GHz transition at different magnetic fields (corrected for offset). The saturated traces are coded in dark blue. As time evolves the color changes to red.

4 Results

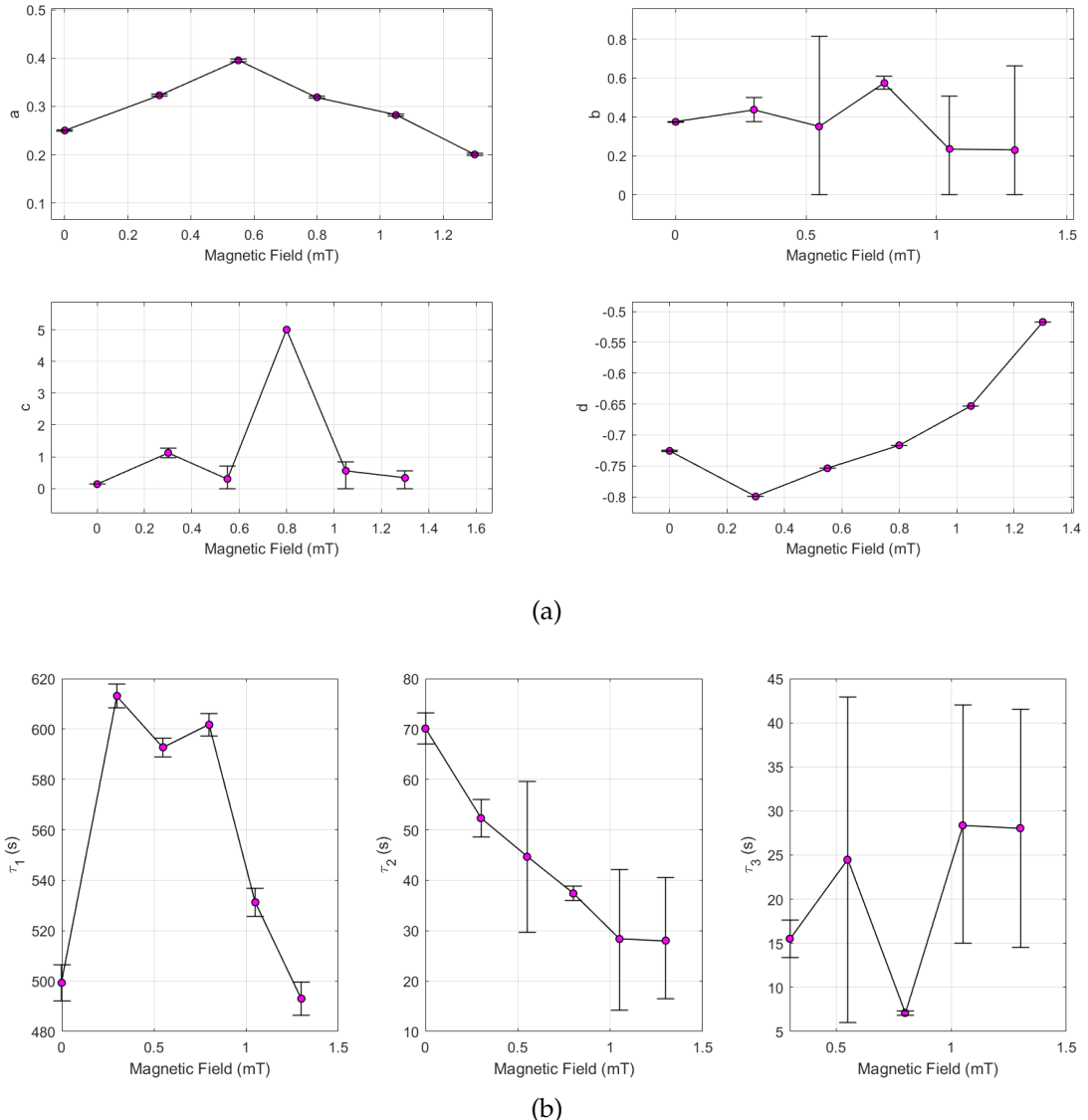


Figure 4.10: Fit parameters at different magnetic fields. (a) shows the amplitude coefficients (a, b, c, d) of the fitting function with a truncated lower limit of the error bar at 0 due to physical constraints. Subfigure (b) shows the time constants of the exponential (τ_1, τ_2, τ_3), which represent the T_1 relaxation times of the system.

4 Results

Lastly, the parameter d represents the relaxed absorption area, which is the total absorbed intensity once the spin system has reached thermal equilibrium. As shown in Figure 4.10, d increases with magnetic field strength. This trend corresponds to a reduction in maximum absorption, which is also evident in Figure 4.9 through the decreasing depth of the absorption dips. A plausible physical explanation for this behavior is field-induced broadening of the spin transitions and changes in transition probabilities.

CHAPTER 5

Conclusion

The study of spin-ensembles based on rare-earth ions doped in crystals is an important step in developing quantum memories for hybrid quantum systems in the microwave regime. In this work, we have conducted an experimental study on erbium-doped calcium tungstate (Er:CaWO_4) at sub-kelvin temperatures.

Using electron spin resonance (ESR) experiments with superconducting circuits under sub-kelvin conditions, we have experimentally studied the spin transitions of $^{167}\text{Er:CaWO}_4$. The 167 isotope of erbium has a nuclear spin value of $I = 7/2$ and an electron spin value of $S = 1/2$. Their coupling gives rise to the hyperfine interaction and nuclear quadrupole interaction terms in the spin Hamiltonian, which are both generally independent of the field. Thus, in zero-field conditions, only hyperfine transitions of the sample can be observed. These hyperfine transitions have been detected and shown using spectroscopy experiments done in zero field conditions described in section 4.1.

By conducting field sweeps, we could observe how the external magnetic fields affect the spin transition frequencies when the magnetic field (B_0) is oriented parallel to the microwave propagation vector (\mathbf{k}) and perpendicular to the crystal c-axis. Several conclusions could be drawn from the results of the field sweep. At low fields, the presence of the Zeeman interaction is relatively insignificant and acts as a small perturbation on the hyperfine structure. This could be observed from the small shifts of the hyperfine transitions as the magnetic fields change. However, as the field gets higher, the Zeeman effect will start to dominate over the hyperfine transitions. This was visualized in sweeps up to 30 mT, where we can observe the Zeeman line. Linear fitting of the Zeeman line provides a rough value for the g-factor, which is in line with

5 Conclusion

reported values in the literature.

The saturation recovery measurements conducted under the influence of various external magnetic field strengths have provided significant insights into the relaxation dynamics of our measured sample. Through a systematic investigation of the sample, several points can be summarized. In various measurements at magnetic fields ranging from zero-field to 1.3 mT, we have observed consistently long relaxation times for the 2.6 GHz transition, with the spin system requiring multiple hundreds of seconds to fully relax to its thermal equilibrium state. Difficulties arise when trying to conduct saturation recovery experiments at higher fields due to the very weak absorption depth, which causes the noise from the background to overpower the absorption dip at the spin transition. A long T_1 relaxation time of hyperfine transitions indicates less energy loss, which helps preserve the quantum state for longer periods of time.

List of Figures

2.1	Unit Cell of Calcium Tungstate	6
2.2	Energy Structure of ^{167}Er	7
2.3	Bloch Sphere	10
3.1	Coplanar Waveguide	14
3.2	Measurement Setup	16
3.3	Two Port VNA and S-Parameters	17
3.4	Microwave Power Sweep	19
3.5	Saturation Recovery Measurement	20
4.1	Broadband Spectroscopy of Er:CaWO ₄ from 100 MHz to 4 GHz in zero-field.	22
4.2	Zero-field spectroscopy of hyperfine transitions	23
4.3	Magnetic Field Sweep from -2 mT to -30 mT	25
4.4	Near zero-field high resolution sweep	26
4.5	Lineshape Curve in Complex Plane	28
4.6	Original vs Corrected Data	29
4.7	Decay of $-\alpha L$ of the 2.6 GHz transition in zero-field	30
4.8	Integral of $-\alpha L$ as a function of time and fitted tri-exponential curve . .	31
4.9	$-\alpha L$ of the decay measurement at different magnetic fields	34
4.10	Fit parameters at different magnetic fields	35

List of Tables

2.1 Lanthanides	5
2.2 Spin Hamiltonian Parameters	9
4.1 Zeeman line fitting	25
4.2 Decay Fitting Parameters	32
4.3 Magnetic field vs. center frequency	32

Bibliography

- [1] R. Blatt, H. Häffner, C. Roos, C. Becher, and F. Schmidt-Kaler. “Course 5 - Quantum Information Processing in Ion Traps I.” In: *Quantum Entanglement and Information Processing*. Ed. by D. Estève, J.-M. Raimond, and J. Dalibard. Vol. 79. Les Houches. Elsevier, 2004, pp. 223–260. doi: [https://doi.org/10.1016/S0924-8099\(03\)80029-X](https://doi.org/10.1016/S0924-8099(03)80029-X).
- [2] C. Clauss. “On-Chip Broadband Magnetic Resonance Spectroscopy Down to Ultralow Temperatures.” PhD Thesis. Universität Stuttgart, 2014.
- [3] C. Clauss, D. Bothner, D. Koelle, R. Kleiner, L. Bogani, M. Scheffler, and M. Dressel. “Broadband electron spin resonance from 500MHz to 40GHz using superconducting coplanar waveguides.” In: *Applied Physics Letters* 102.16 (Apr. 2013). issn: 1077-3118. doi: 10.1063/1.4802956.
- [4] E. Z. Cruzeiro, A. Tiranov, I. Usmani, C. Laplane, J. Lavoie, A. Ferrier, P. Goldner, N. Gisin, and M. Afzelius. “Spectral hole lifetimes and spin population relaxation dynamics in neodymium-doped yttrium orthosilicate.” In: *Phys. Rev. B* 95 (20 May 2017), p. 205119. doi: 10.1103/PhysRevB.95.205119.
- [5] M. L. Dantec, M. Rančić, S. Lin, E. Billaud, V. Ranjan, D. Flanigan, S. Bertaina, T. Chanelière, P. Goldner, A. Erb, R. B. Liu, D. Estève, D. Vion, E. Flurin, and P. Bertet. *Twenty-three millisecond electron spin coherence of erbium ions in a natural-abundance crystal*. 2021. arXiv: 2106.14974 [quant-ph].
- [6] E. Dikarov, O. Zgadzai, Y. Artzi, and A. Blank. “Direct Measurement of the Flip-Flop Rate of Electron Spins in the Solid State.” In: *Phys. Rev. Appl.* 6 (4 Oct. 2016), p. 044001. doi: 10.1103/PhysRevApplied.6.044001.
- [7] M. Göppl, A. Fragner, M. Baur, R. Bianchetti, S. Filipp, J. M. Fink, P. J. Leek, G. Puebla, L. Steffen, and A. Wallraff. “Coplanar waveguide resonators for circuit quantum electrodynamics.” In: *Journal of Applied Physics* 104.11 (2008), p. 113904. doi: 10.1063/1.3010859.

Bibliography

- [8] C. Grezes, B. Julsgaard, Y. Kubo, M. Stern, T. Umeda, J. Isoya, H. Sumiya, H. Abe, S. Onoda, T. Ohshima, V. Jacques, J. Esteve, D. Vion, D. Esteve, K. Mølmer, and P. Bertet. "Multimode Storage and Retrieval of Microwave Fields in a Spin Ensemble." In: *Phys. Rev. X* 4 (2 June 2014), p. 021049. doi: 10.1103/PhysRevX.4.021049.
- [9] C. Grezes, Y. Kubo, B. Julsgaard, T. Umeda, J. Isoya, H. Sumiya, H. Abe, S. Onoda, T. Ohshima, K. Nakamura, I. Diniz, A. Auffeves, V. Jacques, J.-F. Roch, D. Vion, D. Esteve, K. Moelmer, and P. Bertet. "Towards a spin-ensemble quantum memory for superconducting qubits." In: *Comptes Rendus. Physique* 17.7 (July 2016), pp. 693–704. issn: 1878-1535. doi: 10.1016/j.crhy.2016.07.006.
- [10] M. Guo, S. Liu, W. Sun, et al. "Rare-earth quantum memories: The experimental status quo." In: *Frontiers of Physics* 18 (2023), p. 21303. doi: 10.1007/s11467-022-1240-8.
- [11] K. Jing, Z. Lan, Z. Shi, S. Mu, X. Qin, X. Rong, and J. Du. "Broadband electron paramagnetic resonance spectrometer from 1 to 15 GHz using metallic coplanar waveguide." In: *Review of Scientific Instruments* 90.12 (2019), p. 125109. doi: 10.1063/1.5119333.
- [12] P. Krantz, M. Kjaergaard, F. Yan, T. P. Orlando, S. Gustavsson, and W. D. Oliver. "A quantum engineer's guide to superconducting qubits." In: *Applied Physics Reviews* 6.2 (June 2019). issn: 1931-9401. doi: 10.1063/1.5089550.
- [13] M. Le Dantec. "Electron spin dynamics of erbium ions in scheelite crystals, probed with superconducting resonators at millikelvin temperatures." PhD Thesis. Université Paris-Saclay, Jan. 2022.
- [14] H. Malissa, D. I. Schuster, A. M. Tyryshkin, A. A. Houck, and S. A. Lyon. "Superconducting coplanar waveguide resonators for low temperature pulsed electron spin resonance spectroscopy." In: *Review of Scientific Instruments* 84.2 (2013), p. 025116. doi: 10.1063/1.4792205.
- [15] S. Probst, F. B. Song, P. A. Bushev, A. V. Ustinov, and M. Weides. "Efficient and robust analysis of complex scattering data under noise in microwave resonators." In: *Review of Scientific Instruments* 86.2 (Feb. 2015). issn: 1089-7623. doi: 10.1063/1.4907935.
- [16] S. Probst. "Hybrid quantum system based on rare earth doped crystals = Hybrides Quantensystem basierend auf Kristallen mit Seltenerddotierung." PhD thesis. 2015. doi: 10.5445/IR/1000045286.

Bibliography

- [17] M. Rančić, M. Le Dantec, S. Lin, S. Bertaina, T. Chanelière, D. Serrano, P. Goldner, R. B. Liu, E. Flurin, D. Estève, D. Vion, and P. Bertet. “Electron-spin spectral diffusion in an erbium doped crystal at millikelvin temperatures.” In: *Phys. Rev. B* 106 (14 Oct. 2022), p. 144412. doi: 10.1103/PhysRevB.106.144412.
- [18] P. M. Schosseler. “Electron paramagnetic resonance study of the copper(II) complexation with carbonate ligands in aqueous solution and at calcium carbonate surfaces.” en. Diss. Naturwiss. ETH Zürich, Nr. 12669, 1998. Ref.: A. Schweiger ; Korref.: B. Wehrli. Doctoral Thesis. Zürich: ETH Zurich, 1998. doi: 10.3929/ethz-a-001935980.
- [19] R. N. Simons. *Coplanar Waveguide Circuits, Components, and Systems*. John Wiley & Sons, Inc., 2001. ISBN: 9780471161219. doi: 10.1002/0471224758.
- [20] A. Strinic, P. Oehrl, A. Marx, P. A. Bushev, H. Huebl, R. Gross, and N. Kukharchyk. “Broadband electron paramagnetic resonance spectroscopy of $^{167}\text{Er}:\text{LiYF}_4$ at mK temperatures.” In: (2025). arXiv: 2501.04657 [quant-ph].
- [21] H. Syed, A. Kinos, C. Shi, L. Rippe, and S. Kröll. “Microscopic model of spin flip-flop processes in crystals doped by rare-earth ions.” In: *Physical Review B* 106.18 (Nov. 2022). ISSN: 2469-9969. doi: 10.1103/physrevb.106.184109.
- [22] G. Wendin. “Quantum information processing with superconducting circuits: a review.” In: *Reports on Progress in Physics* 80.10 (Sept. 2017), p. 106001. doi: 10.1088/1361-6633/aa7e1a.
- [23] J. Yang, W. Fan, Y. Zhang, C. Duan, G. G. de Boo, R. L. Ahlefeldt, J. J. Longdell, B. C. Johnson, J. C. McCallum, M. J. Sellars, S. Rogge, C. Yin, and J. Du. “Zeeman and hyperfine interactions of a single $^{167}\text{Er}^{3+}$ ion in Si.” In: *Physical Review B* 105.23 (June 2022). ISSN: 2469-9969. doi: 10.1103/physrevb.105.235306.

Acknowledgments

In this section, I would like to express my gratitude to everyone who has enabled me to complete this work and who has supported me throughout my bachelor's studies. First and foremost, I thank Prof. Dr. Kai Müller for agreeing to be my formal university supervisor for this externally conducted project at the Walther-Meissner Institute (WMI).

I am also especially grateful to my supervisors at WMI, Dr. Nadezhda Kukharchyk and Georg Mair, for warmly welcoming me into the Microwave Rare Earth Systems research group, guiding me through each stage of the project, and providing generous feedback during the writing process. I am especially thankful for the chance to learn and pursue my interests in an experimental physics lab, despite coming from an engineering background. Furthermore, I would like to thank the entire WMI staff and other fellow students in the lab with whom I have had the pleasure of working for a few months.

On the other hand, I would also like to thank all my friends and colleagues who have supported me not only through the process of this thesis but also throughout my Bachelor's studies. Thank you for the learning, discussions, feedback, and the many running sessions that have kept me sane. Last but not least, I want to thank my family back home for their unrelenting support these past few years.